

**AN INVESTIGATION OF THE MAGNETO-TRANSPORT  
AND SUPERCONDUCTING PROPERTIES OF  
HALF HEUSLER THIN FILMS**

**SHIVANGI SRIVASTAVA**



**DEPARTMENT OF PHYSICS  
INDIAN INSTITUTE OF TECHNOLOGY DELHI  
SEPTEMBER 2025**

© Indian Institute of Technology Delhi (IITD), New Delhi, 2025

**An Investigation of the Magneto-Transport and  
Superconducting Properties of Half Heusler Thin  
Films**

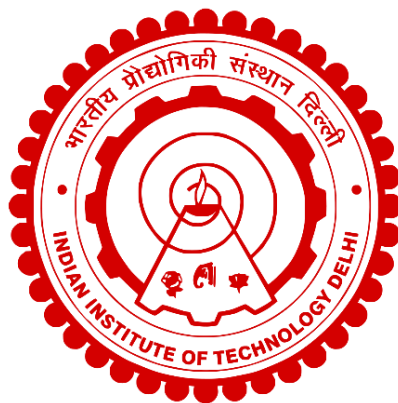
*by*

**Shivangi Srivastava**  
**DEPARTMENT OF PHYSICS**

*Submitted*

*In fulfilment of the requirement of the degree of*

**Doctor of Philosophy**



**INDIAN INSTITUTE OF TECHNOLOGY DELHI**

**SEPTEMBER 2025**

## **DEDICATION**

This thesis is lovingly dedicated to my papa, Late Dr. Prabha Shankar

(my hero, my strength, my role model).

It was his unfulfilled dream to reach the pinnacle of academic pursuit, to earn the highest degree in science. Though he is no longer here to witness this moment, every step of this journey has been carried on the foundation of his unwavering support, quiet sacrifices, and the values he instilled in me.

He taught me to move forward with courage, hope, and a heart full of positivity, even in the darkest of times. His values and principles became my strength. His dreams became my purpose.

I feel his presence in every heartbeat, every achievement, and I know, somewhere beyond this world, he is smiling with pride.

This accomplishment is not mine alone; it is his. With all my love and the deepest gratitude, I offer it to him.

“Love you, Papa.”



**Department of Physics  
Indian Institute of Technology  
Delhi Hauz Khas, India-110016**

---

### **Certificate**

This is to certify that this thesis entitled "**An Investigation of the Magneto-Transport and Superconducting Properties of Half Heusler Thin Films**" being submitted by **Ms. Shivangi Srivastava** to the Indian Institute of Technology Delhi for the award of the degree of "**Doctor of Philosophy (Ph.D.)**", is a record of bonafide research work carried out under my guidance and supervision. The work or any part of the thesis have not been submitted in part or full to any other University or Institute for award of any degree or diploma.

#### **Supervisor**

**Prof. Ratnamala Chatterjee**  
Department of Physics  
Indian Institute of Technology Delhi  
India - 110016.

## **Declaration**

I certify that

- a. The work contained in the thesis is original and has been done by me under the guidance of my supervisor;
- b. The work has not been submitted to any other institute for any other degree or diploma;
- c. I have followed the guidelines provided by the Institute in preparing the thesis;
- d. I have conformed to ethical norms and guidelines while writing the thesis;
- e. Whenever I have used materials (data, models, figures and text) from other sources, I have given due credit to them by citing them in the text of the thesis, and giving their details in the references, and taken permission from the copyright owners of the sources, whenever necessary.

**Shivangi Srivastava**

## ACKNOWLEDGMENTS

*With deep reverence, I bow to Lord Krishna, the supreme guide in my life.*

I sincerely thank everyone who has supported me throughout my academic journey. Without their direct and indirect contributions, reaching this milestone would not have been possible. While it is difficult to name everyone individually, I would like to express my heartfelt gratitude to a few key individuals.

First and foremost, I express my deepest thanks to my teacher and supervisor, Prof. Ratnamala Chatterjee, for her unwavering guidance, encouragement, and trust in me. Her insights and support, especially during challenging times, kept me focused and motivated to give my best.

I am equally grateful to my SRC members, Prof. Pankaj Srivastava, Prof. Sujit Manna, and Prof. Debanjan Bhowmik, for their valuable discussions and mentorship, which helped shape my scientific thinking and sharpen my presentation skills.

I feel fortunate to have worked with inspiring collaborators, Late Prof. Vinay Gupta, Prof. Aftab Alam and Dr. Niladari Banerjee, whose expertise and perspectives enriched my research.

I gratefully acknowledge the Central Research Facilities (CRF), Nanoscale Research Facilities (NRF), and the Department of Physics, IIT Delhi, for providing me with the infrastructure and support necessary for my research. I also thank the Ministry of Education, Government of India, and IIT Delhi for the financial support and opportunities to attend conferences and workshops both in India and abroad. I am also thankful to IIT Delhi for providing financial support through the Institute Fellowship.

To my lab mates, Dr. Devendra Pandey, Dr. Mithun Majhi, Dr. Deepika Rani, Dr. Vishal Bhardwaj, Dr. Divya Prakash Dubey, Dr. Anupam Bhattacharya, Dr. Hitesh Gulati, Dr. Priyanka Sharma, Dr. Durgesh Ojha, Vikas Chahar, Balwant Chauhan, and Rinku, thank you for your companionship, support, and encouragement throughout the Ph.D. journey. A special thanks to Dr. Risabh Shukla, who has stood by me since my master's days, offering constant support and positivity.

To my dear friends who became family at IIT Delhi, Dr. Ranjana, Dr. Vandana, and Shobha, thank you for the shared weekends, comforting food, endless conversations, and

unforgettable memories. Your support during difficult times and your patience with my sarcasm meant more than words can say.

I deeply cherish the love and encouragement from my school and college friends at BHU and IIT Kanpur, who celebrated every small and big success of mine with genuine happiness.

Words cannot express the immense love and gratitude I have for my mother, Dr. Vandana Srivastava, my sister, Dr. Trishla Srivastava, and my brother, Dr. Trishek Srivastava, for their constant belief in me and for being my unwavering pillars of strength throughout this journey and beyond.

My heartfelt thanks to my family and my extended family, especially my sister-in-law, Shikha Sharma, whose motherly care for my toddler during the most demanding phase of thesis writing was a true blessing. Her selfless support played a crucial role in the completion of this journey.

This journey would have been much more difficult without the unwavering support of my husband, Dr. Suraj Prakash. I feel truly blessed to have him by my side through every phase, from M.Sc. to Ph.D., and beyond. His constant encouragement, strength, and wisdom inspired me to keep moving forward. I am deeply grateful for his love, patience, and belief in my dreams.

Finally, my utmost and most special thanks to my son, Shivank Madhav, whose birth brought light into my life. His innocent smile wipes away every sorrow, and his presence fills my heart with boundless joy and completeness. I thank him for choosing me as his mother.

Shivangi Srivastava

## ABSTRACT

This thesis presents a systematic investigation of the magneto-transport, superconducting, and topological properties of doped and strained half-Heusler (HH) thin films based on rare-earth alloys. The study focuses on three alloy systems: (i) Er-doped YPdBi, (ii) Y-doped HoPdBi, and (iii) strained GdPdBi, grown using pulsed laser deposition (PLD), with the aim of tuning their electronic structure via  $f$ -electron doping, magnetic dilution, and lattice strain.

The first part of this thesis investigates the  $Y_{1-x}Er_xPdBi$  ( $x = 0.2(E2), 0.5(E5), 0.8(E8)$ ) thin films to study the effect of  $f$ -electron doping on the otherwise topologically trivial, diamagnetic YPdBi. All the films exhibit semimetallic behavior with clear signatures of superconductivity at low temperatures. The optimally doped E5 film ( $x = 0.5$ ) showed a maximum superconducting transition temperature ( $T_c \sim 4.4$  K), with a high quantum mobility, and a large phase coherence length. While E2 and E8 films exhibited  $T_c$  values of  $\sim 2.2$  K and  $\sim 3.7$  K, respectively. Detailed magneto-transport measurements revealed features characteristic of non-trivial topological materials, such as weak anti-localization (WAL) and Shubnikov–de Haas (SdH) oscillations. The power law fitting of phase coherence lengths, the extracted  $\alpha$  value confirmed the presence of 2D surface state. The extracted Berry phase ( $\sim \pi$ ) confirmed the presence of Dirac fermions. First-principles DFT calculations validated the non-trivial topological band ordering in all compositions, with band inversion strength increasing with Er content due to  $s$ - $f$  exchange interactions. The optimally doped film (E5) showed enhanced quantum coherence and mobility, attributed to more  $f$  bands near the Fermi level. These findings indicate that Er-doped YPdBi thin films exhibit a strong interplay between superconductivity and topological band structure.

The second part investigates  $Ho_{1-x}Y_xPdBi$  ( $x = 0(Y2), 0.2(Y2), 0.8(Y8)$ ) thin films, where substitution of magnetic  $Ho^{3+}$  ions by non-magnetic  $Y^{3+}$  modifies both magnetism and transport characteristics. Electrical resistivity measurements revealed semimetallic nature and superconducting transitions in all films, with the  $x=0.8$  (Y8) film achieving a zero-resistivity state at  $T_c \sim 2.8$  K. While Y0 and Y2 films exhibited  $T_c$  values of  $\sim 0.9$  K and  $\sim 2.1$  K, respectively Bulk superconductivity in the Y8 film was confirmed through AC susceptibility measurements, showing a strong diamagnetic response and an upper critical field  $H_{c2}(0) \sim 5.7$  T. Magneto-resistance measurements displayed weak anti-

localization (WAL)-like behavior at low fields. Using HLN model, the  $\alpha$  and  $l_\phi$  value extracted. The unphysical value of  $\alpha$  at different temperatures and value of  $l_\phi(4K) <$  thickness of HYPB films, which reflects that WAL originates from 3D bulk conduction.  $l_\phi$  analysis revealed that *electron–electron (e–e)* scattering dominates in Y0 and Y8 films, while the Y2 film exhibited additional *electron–phonon (e–ph) scattering*, suggesting a coexistence of scattering mechanism.

In the final part, the structural and transport properties of GdPdBi thin films were explored under  $\sim 1\%$  strain. X-ray diffraction and microscopic analyses confirm high-quality, single-phase films with  $\sim 1\%$  lattice strain relative to the bulk. Temperature-dependent resistivity measurements reveal a two conducting behaviour: metallic behavior ( $T < 3.5K$ ), and semiconducting behavior ( $T > 3.5K$ ) with a reduced energy gap of  $\sim 10.2$  meV, significantly smaller than the bulk band gap ( $\sim 70$  meV), indicating strain-induced band narrowing in the films. Magneto-resistance measurements displayed weak anti-localization (WAL)-like behavior at low fields. HLN model analysis gives unphysical  $\alpha$ -values and coherence lengths smaller than the film thickness, indicating that WAL originates from 3D bulk conduction. Angle-dependent magneto-conductance measurements confirmed that the observed WAL-like features originated from 3D bulk states due to spin-orbit coupling (SOC), not from 2D surface states.

Overall, this thesis demonstrates that *f*-electron doping, magnetic dilution, and lattice strain are effective tuning parameters for manipulating the quantum transport and topological properties of HH thin films. These findings provide valuable insights into the design of topological superconductors and pave the way for future applications in spintronics, quantum computation, and topological device platforms.

## सारांश

यह शोधप्रबंध दुर्लभ-पृथ्वी मिश्रधातुओं पर आधारित डोपड और तनावित हाफ-ह्यूस्लर (HH) पतली परतों (thin films) के चुम्बकीय-परिवहन, अतिचालक (superconducting) और टोपोलॉजिकल गुणों की एक व्यवस्थित जाँच प्रस्तुत करता है। अध्ययन तीन मिश्रधातु प्रणालियों पर केंद्रित है: (i) Er-डोपड YPdBi, (ii) Y-डोपड HoPdBi, और (iii) तनावित GdPdBi। इन्हें पल्सड लेज़र निक्षेपण (PLD) तकनीक से विकसित किया गया है, जिसका उद्देश्य  $f$ -इलेक्ट्रॉन डोपिंग, चुम्बकीय पतला करना (magnetic dilution), और लैटिस तनाव के माध्यम से इनके इलेक्ट्रॉनिक संरचना को नियंत्रित करना है।

शोधप्रबंध का पहला भाग  $Y_{1-x}Er_xPdBi$  ( $x = 0.2(E2), 0.5(E5), 0.8(E8)$ ) पतली परतों की जाँच करता है ताकि  $f$ -इलेक्ट्रॉन डोपिंग के प्रभाव का अध्ययन किया जा सके, जो सामान्यतः टोपोलॉजिकल रूप से तुच्छ और प्रतिचुम्बकीय (diamagnetic) YPdBi पर लागू होता है। सभी फिल्मों में अर्ध-धात्विक (semimetallic) व्यवहार प्रदर्शित करती हैं और निम्न तापमान पर अतिचालकता (superconductivity) के स्पष्ट संकेत देती हैं। E5 ( $x = 0.5$ ) फिल्म ने अधिकतम अतिचालक संक्रमण तापमान ( $\sim 4.4$  K) दर्शाया, साथ ही उच्च क्वांटम गतिशीलता (mobility) और बड़ी चरण-समरूपता लंबाई (phase coherence length) दिखाई। वहीं E2 और E8 फिल्मों ने क्रमशः  $\sim 2.2$  K और  $\sim 3.7$  K के  $T_c$  मान प्रस्तुत किए। विस्तृत मैग्नेटो-ट्रांसपोर्ट मापनों ने टोपोलॉजिकल पदार्थों की विशिष्ट विशेषताओं, जैसे कि कमजोर प्रतिलोकीकरण (weak anti-localization, WAL) और शुभ्निकोव-डी हास (SdH) दोलन, को उजागर किया। चरण-समरूपता लंबाई के पावर-लॉ विश्लेषण से 2D सतही अवस्था की उपस्थिति की पुष्टि हुई। निकाली गई बेरी फेज़ ( $\sim \pi$ ) ने डिराक फ़र्मियोन्स की उपस्थिति को सत्यापित किया। प्रथम-सिद्धांत DFT गणनाओं ने बैंड उलटफेर (band inversion) के साथ गैर-तुच्छ टोपोलॉजिकल बैंड क्रम की पुष्टि की, जो Er मात्रा के बढ़ने के साथ  $s-f$  विनिमय क्रियाओं द्वारा प्रबलित हुआ। विशेष रूप से E5 फिल्म ने अधिक  $f$ -बैंड्स के फ़र्मी स्तर के समीप होने से, उन्नत क्वांटम समरूपता और गतिशीलता प्रदर्शित की। यह दर्शाता है कि Er-डोपड YPdBi पतली परतों में अतिचालकता और टोपोलॉजिकल बैंड संरचना के बीच मजबूत अंतःक्रिया होती है।

शोध का दूसरा भाग  $Ho_{1-x}Y_xPdBi$  ( $x = 0(Y0), 0.2(Y2), 0.8(Y8)$ ) पतली परतों पर केंद्रित है, जहाँ चुम्बकीय  $Ho^{3+}$  आयनों को अचुम्बकीय  $Y^{3+}$  आयनों से प्रतिस्थापित करने से चुम्बकत्व और

परिवहन गुण दोनों में परिवर्तन आता है। विद्युत प्रतिरोधकता ने सभी फिल्मों में अर्ध-धात्विक प्रकृति तथा अतिचालक संक्रमण दिखाया। विशेष रूप से  $x=0.8$  (Y8) फिल्म ने  $\sim 2.8$  K पर शून्य प्रतिरोधात्मक अवस्था प्राप्त की, जबकि Y0 और Y2 फिल्मों के लिए यह मान क्रमशः  $\sim 0.9$  K और  $\sim 2.1$  K रहा। Y8 फिल्म में बल्क अतिचालकता को AC सुसेप्टिबिलिटी मापन द्वारा पुष्टि मिली, जिसमें प्रबल प्रतिचुम्बकीय प्रतिक्रिया और 5.7 T तक का उच्चतम क्रांतिक क्षेत्र (upper critical field) पाया गया। मैग्नेटो-रेसिस्टेंस मापनों में निम्न क्षेत्रों पर WAL जैसी विशेषताएँ दिखाई दीं। HLN मॉडल से प्राप्त मानों ने दर्शाया कि WAL मुख्य रूप से 3D बल्क कंडक्शन से उत्पन्न होता है। साथ ही, विश्लेषण से स्पष्ट हुआ कि Y0 और Y8 फिल्मों में मुख्यतः इलेक्ट्रॉन-इलेक्ट्रॉन प्रकीर्णन ( $e-e$  scattering) प्रभावी है, जबकि Y2 फिल्म में इसके अतिरिक्त इलेक्ट्रॉन-फोनॉन ( $e-ph$ ) प्रकीर्णन भी मौजूद है, जो मिश्रित प्रकीर्णन तंत्र की उपस्थिति का संकेत देता है।

अंतिम भाग में,  $\sim 1\%$  तनाव के अधीन GdPdBi पतली परतों की संरचनात्मक और परिवहन विशेषताओं का अध्ययन किया गया। एक्स-रे विवर्तन और सूक्ष्मदर्शी विश्लेषणों ने बल्क की तुलना में  $\sim 1\%$  लैटिस तनाव वाली एकल-चरण व उच्च गुणवत्ता वाली फिल्मों की पुष्टि की। ताप-निर्भरता अध्ययन में द्वि-चालकता (dual conducting) व्यवहार देखा गया—उच्च तापमान पर धात्विक व्यवहार और  $T < \sim 3.5$  K पर अर्धचालक व्यवहार। यहाँ ऊर्जा गैप  $\sim 10.2$  meV मापा गया, जो बल्क गैप ( $\sim 70$  meV) से काफी छोटा है, और यह तनाव-प्रेरित बैंड संकुचन को दर्शाता है। मैग्नेटो-रेसिस्टेंस मापनों ने निम्न क्षेत्रों पर WAL जैसी विशेषताएँ दिखाई। HLN मॉडल का विश्लेषण बताता है कि  $\alpha$ -मूल्य भौतिक रूप से अवास्तविक हैं और समरूपता लंबाई फिल्म की मोटाई से छोटी है, जिससे यह सिद्ध होता है कि WAL 3D बल्क कंडक्शन से उत्पन्न होता है। कोण-निर्भर मैग्नेटो-कंडक्टेंस ने यह पुष्टि किया कि WAL जैसी विशेषताएँ 2D सतही अवस्थाओं से नहीं, बल्कि प्रबल SOC (spin-orbit coupling) के कारण 3D बल्क अवस्थाओं से उत्पन्न हुई थीं।

समग्र रूप से, यह शोधप्रबंध दर्शाता है कि  $f$ -इलेक्ट्रॉन डोपिंग, चुम्बकीय पतलापन, और लैटिस तनाव HH पतली परतों में क्वांटम परिवहन और टोपोलॉजिकल गुणों को नियंत्रित करने के लिए प्रभावी साधन हैं। ये निष्कर्ष टोपोलॉजिकल अतिचालकों के डिज़ाइन में महत्वपूर्ण दृष्टिकोण प्रदान करते हैं और स्पिन्ट्रॉनिक्स, क्वांटम कंप्यूटेशन, एवं टोपोलॉजिकल युक्ति प्लेटफॉर्म में भविष्य के अनुप्रयोगों का मार्ग प्रशस्त करते हैं।

# TABLE OF CONTENT

<b>Certificates</b>	i
<b>Acknowledgement</b>	iii
<b>Abstract</b>	v
<b>Table of Content</b>	ix
<b>List of Figures</b>	xii
<b>List of Tables</b>	xvi

## Chapter 1

<b>1. Introduction</b>	1
1.1 Introduction to Heusler Alloys	2
1.2 Evolution of Topological Concepts in Quantum Phase Materials	5
1.2.1 Quantum Hall Effect	6
1.2.2 Quantum Spin Hall Effect	9
1.3 Realizations of Topological Phases in Materials	11
1.3.1 Spin-orbit Coupling and Band Inversion	11
1.3.2 Time Reversal Symmetry	12
1.4 Topological Classification of Materials	14
1.4.1 Topological Insulators	14
1.4.2 Topological Semimetals	16
1.4.2.1 Dirac Semi-metals	17
1.4.2.2 Weyl Semi-metals	18
1.4.2.3 Nodal-Line Semimetal	19
1.4.3 Topological Superconductors	20
1.5 Probing Topological Nontriviality: Key Observables	20
1.6 Rare Earth-Based Half-Heusler Alloys as Topological Candidates	23
1.7 Research Gap, Motivation, and Thesis Objectives	26
1.8 Thesis Organization	28
References	33

## Chapter 2

<b>2. Experimental Techniques</b>	40
2.1 Sample Preparation Methods	41
2.1.1 Polycrystalline Bulk Sample Preparation Using Modified Rf Induction Melting	41
2.1.2 Thin Film Growth using Pulsed Laser Deposition (PLD)	42

2.2	Sample Characterization Techniques	44
2.2.1	X-Ray Diffraction (XRD)	44
2.2.2	Rocking Curve ( $\omega$ Scan)	46
2.2.3	X-Ray-Reflectivity (XRR)	47
2.2.4	Atomic Force Microscopy (AFM)	48
2.2.5	Scanning Electron Microscopy (SEM)	50
2.2.6	Energy Dispersive X-ray Spectroscopy (EDS)	51
2.3	Measurement Techniques	52
2.3.1	Physical Property Measurement System (PPMS)	52
2.3.1.1	Four-Probe Electrical and Magneto-Transport Measurements	54
2.3.2	Squid Magnetometer	56
	References	58
<b>Chapter 3</b>		
<b>3.</b>	<b>The Effect of <i>f</i>-Electron Doping on Magneto-Transport and Electrical Resistivity of YPdBi Thin Films</b>	<b>59</b>
3.1	Introduction	60
3.2	Experimental Details	61
3.3	Computational Details	62
3.4	Results and Discussions	63
3.5	Conclusion	80
	References	81
<b>Chapter 4</b>		
<b>4.</b>	<b>Investigation of Electrical and Galvano-Magnetic Properties of <math>\text{Ho}_{1-x}\text{Y}_x\text{PdBi}</math> (<math>x=0, 0.2, 0.8</math>) Half Heusler Alloys Thin Films</b>	<b>86</b>
4.1	Introduction	87
4.2	Experimental Details	88
4.3	Results and Discussion	88
4.4	Conclusion	97
	References	98
<b>Chapter 5</b>		
<b>5.</b>	<b>Study of Structural and Magneto-Transport Properties of Ternary Half-Heusler GdPdBi Thin Films</b>	<b>100</b>
5.1	Introduction	101
5.2	Experimental Details	102

5.3	Results and Discussion	104
5.4	Conclusion	109
	References	110
<b>Chapter 6</b>		
<b>6.</b>	<b>Summary and Future Perspective</b>	113
6.1	Summary	114
6.2	Future Perspective	118
	<b>List of Publication</b>	119
	<b>Author's Biography</b>	120

## LIST OF FIGURES

Figure. 1.1	Periodic table presenting general X (red colour), Y (blue colour), and Z (green colour) elements used to form Heusler alloys.	3
Figure. 1.2	Schematic illustration of (a) the Full Heusler structure and (b) the Inverse Heusler structure.	4
Figure. 1.3	Schematic representation of a half-Heusler alloy.	4
Figure. 1.4	(a) Illustration of topology in geometry. (b) Schematic analogy representing the band inversion phenomenon in a topological insulator and its relation to topology in geometry.	5
Figure. 1.5	(a) Schematic of Hall measurement configuration, (b) Quantization of Hall effect, (c) Formation of Landau Levels in presence of magnetic field, (d) Schematic illustrating circular quantized electron orbits in the bulk and skipping cyclotron orbits along the edges of a 2D system under a magnetic field.	7
Figure. 1.6	(a) Schematic of interface between an insulator and a quantum Hall state host a chiral edge state, understood in terms of skipping cyclotron orbits. (b) Edge state connecting conduction band with valence band.	8
Figure. 1.7	Schematic diagrams of Hall effects, (a) quantum Hall effect, (b) quantum anomalous Hall effect and (c) quantum spin Hall effect.	10
Figure. 1.8	Schematic picture of QSHE as a copy of two QHE. (a) The long arrow and short arrow indicate magnetic field and spin polarization directions respectively. (b) A combination of two opposite edge states leads to a quantum spin Hall state without a magnetic field.	10
Figure. 1.9	Illustration of band inversion due to strong SOC.	12
Figure. 1.10	Consequences of TRS on a system.	13
Figure. 1.11	(a–b) Representation of 2D and 3D TIs in real space, illustrating spin-polarized edge state (in 2D) and surface states (3D) confined to the system boundaries. (c–d) Corresponding energy band diagrams in momentum space for 2D and 3D topological insulators, highlighting the emergence of 1D and 2D Dirac cones, respectively. Here, BCB/BVB stands for bulk conduction/valence band.	15
Figure. 1.12	Three-dimensional schematic illustration of the band (blue: conduction; green: valence) structures for (a) a DSM and (b) a WSM. In the DSM, both bands intersect at a Dirac point (yellow). The Dirac point splits into two Weyl points linked on the surface by a Fermi arc (pink)	17
Figure. 1.13	NLSM, in which the valence (blue) and conduction (red) bands intersect along specific lines in momentum space, forming either a ring-shaped loop or a one-dimensional line, indicated by the green circle/line.	19
Figure. 2.1	<b>(a)</b> Schematic representation of RF induction heating, illustrating a copper solenoid (primary coil) surrounding a workpiece (conducting material), where eddy currents are induced to facilitate rapid heating. <b>(b)</b> The RF induction melting setup used in the present study.	42
Figure. 2.2	Schematic of the experimental setup of Pulsed Laser Deposition (PLD) under vacuum or controlled gas pressure conditions.	43
Figure. 2.3	Schematic illustration of Bragg reflection from a specific family of lattice planes separated by a distance $d$ . The incident and reflected X-ray beams are shown for two adjacent planes, with a resulting path difference of $2d \sin \theta$	45
Figure. 2.4	Schematic of movement of X-rays source and detector in (a) Gonio-mode (b) GIXRD mode.	45
Figure. 2.5	Schematic of a rocking curve measurement.	46
Figure. 2.6	Various parameters obtained from the X-ray reflectivity profile.	48

Figure. 2.7	Schematic representation of the atomic force microscope.	49
Figure. 2.8	Schematic of an interaction volume of the incident electron beam and specimen atoms below the surface of the specimen in the SEM	50
Figure. 2.9	Schematic of EDS, depicting the main components of EDS.	52
Figure. 2.10	Actual image of the cryogenic Ltd. CFMS-PPMS system at IITD.	53
Figure. 2.11	Schematic representation of a resistivity measurement set up using CFMS-PPMS system.	54
Figure. 2.12	Schematic representation of four-probe resistivity measurement configuration.	55
Figure. 2.13	The real image of MPMS-3 SQUID magnetometer.	57
Figure. 3.1	(a-c) The room-temperature powder X-ray diffraction pattern (red circles) of polycrystalline samples, with the Rietveld refinement profiles, and the fitted Bragg peak positions, (d) X-ray diffraction pattern of thin films.	63
Figure. 3.2	(a) The simulated (black lines) XRR curves for all 3 thin films, (b)-(d) represents the AFM image giving the surface roughness of films as, $\sim 4.2$ nm (E2), $\sim 2.1$ nm (E5) and $\sim 5.1$ nm (E8) sample respectively.	64
Figure. 3.3	EDS analysis of the E2, E5 and E8 thin films: (a) on film surface of E2, (b) on film surface of E5; (c) on film surface of E8, respectively. Insets: the FESEM elemental distribution table of films surfaces.	65
Figure. 3.4	(a) The $\rho_{xx}$ versus $T$ plot for thin films in the temperature range of $2\text{ K} \leq T \leq 10\text{ K}$ at zero magnetic field for E2, E5, and E8 films, (b) Low temperature dependence of dc magnetic susceptibility under magnetic field of 50Oe in ZFC for E5 thin film. Inset: Magnetization vs magnetic field at low temperature under ZFC.	65
Figure. 3.5	AC-susceptibility of polycrystalline samples E2, E5 and E8 for driving fields of 0.1Oe with the frequency of 317Hz (a) Real part ( $\chi'_{ac}$ ), (b) Imaginary part ( $\chi''_{ac}$ ).	66
Figure. 3.6	(a) DC magnetic measurement under a magnetic field of 50Oe in ZFC of Ta(5nm)/MgO substrate, (b) M-H data of E5 film at 2K.	67
Figure. 3.7	The field dependent longitudinal resistivity $\rho_{xx}(T)$ vs magnetic field (a) E5 sample, (b) E8 sample, (c-d) show $H_{C2}(0)$ for E5 and E8 films, solid black line represents the linear fit. Inset: shows the G-L fit of E5 and E8 films.	68
Figure. 3.8	(a) MR data of E2, E5, and E8 at 6 K. (b) The HLN fitted parameters ( $\alpha$ , $L_{\phi}$ ) as a function of Er doping concentration ( $x$ ) of E2 ( $x=0.2$ ), E5 ( $x=0.5$ ), and E8 ( $x=0.8$ ) films at 6 K.	69
Figure. 3.9	(a-c) MR data of E2, E5, and E8 samples in the magnetic field of range $-14T \leq H(T) \leq 14T$ , respectively at $T > T_c$ .	70
Figure. 3.10	(a-c) HLN fitting to magneto-conductance data of E2, E5, and E8 samples at different temperatures, respectively.	70
Figure. 3.11	(a-c) Power law dependence of $L_{\phi}$ with temperature of E2, E5 and E8 film respectively.	71
Figure. 3.12	SdH oscillations, $\Delta R_{xx}$ Vs $1/B$ plots for (a) E2, (b) E5, and (c) E8 films, (d)-(f) a fitting of SdH oscillation amplitude to LK formula at constant magnetic; Insets depict the FFT amplitudes vs frequency plots of E2, E5, and E8 films.	72
Figure. 3.13	Using a semi-log Dingle plot at the lowest temperature, the Dingle temperature $T_D$ is extracted for E2, E5 and E8 films, respectively.	73
Figure. 3.14	(a-c) Landau Level Fan Diagram which is the plot of the LL indices with the reciprocal magnetic fields, the intercept of extrapolated linear fit on n-axis gives Berry phase ( $2\pi\beta$ ) for E2 $\sim 0.98\pi$ , E5 $\sim 0.92\pi$ , and E8 $\sim 0.86\pi$ , respectively.	74
Figure.. 3.15	Crystal structure of $Y_{1-x}Er_xPdBi$ shown in (a) cubic conventional cell (left) and $2 \times 2 \times 2$ supercell of the primitive unit cell of fcc lattice (right) along with AFM2 ordering. The arrows denote the direction of magnetic moments on Er atoms. Bulk band structure of $Y_{1-x}Er_xPdBi$ at experimental bulk lattice parameters for (b) $x = 0$ , (c) $x = 1$ , (d) $x = 0.25$ , (e) $x = 0.50$ and (f) $x = 0.75$ with $s$ -like and $p$ -like atomic	75

	orbital projections. (g) Primitive bulk 3D Brillouin zone with bulk high symmetry points and (112) surface projected 2D Brillouin zone with corresponding surface high symmetry points. Surface dispersion of $Y_{1-x}Er_xPdBi$ at strained thin-film lattice parameters for (h) $x = 0.25$ , (i) $x = 0.50$ and (j) $x = 0.75$ with spectral weights denoting the surface contribution of electronic bands.	
Figure. 3.16	Simulation unit cell of $Y_{1-x}Er_xPdBi$ (a) for $x = 0$ , (b) for $x = 0.25$ , (c) for $x = 0.50$ , (d) for $x = 0.75$ and (e) for $x = 1$ with base AFM2 ordering. The arrows denote the direction of magnetic moments on Er atoms.	77
Figure. 3.17	(a) Conventional cubic cell of $ErPdBi$ . Simulated magnetic orderings with only the magnetic atoms (Er) shown in the conventional cell for (b) FM, (c) AFM1, (d) AFM2 [shown in $2 \times 2 \times 2$ supercell of conventional cell] and (e) AFM3 [shown in $2 \times 1 \times 1$ supercell of conventional cell] configurations. The arrows denote the direction of magnetic moments on Er atoms.	77
Figure. 3.18	Bulk band structure of $Y_{1-x}Er_xPdBi$ (a) for $x = 0.25$ , (b) for $x = 0.50$ and (c) for $x = 0.75$ with base AFM2 ordering at strained thin-film lattice parameters.	79
Figure 4.1	(a-c) The room-temperature powder X-ray diffraction pattern (red circles) of $Ho_{1-x}Y_xPdBi$ ( $x = 0, 0.2$ , and $0.8$ ) bulk sample, with the Rietveld refinement profiles, the fitted Bragg peak positions, (d-f) X-ray diffraction pattern of thin films indicating the presence of (110) symmetrical Bragg's reflections only. The inset shows the rocking curve ( $\theta/2\theta$ ) of (220) peak.	89
Figure. 4.2	(a-f) show the cross-sectional EDX mapping of $HoPdBi$ film; (g) the thickness of $HoPdBi$ (Y0) film shown in cross-sectional view of FESEM image $\sim 111$ nm.	89
Figure. 4.3	The cross-sectional view of FESEM image with thickness of (a) $Ho_{0.8}Y_{0.2}PdBi$ film (Y02) $\sim 119$ nm, (b) $Ho_{0.2}Y_{0.8}PdBi$ film (Y08) $\sim 120$ nm.	90
Figure. 4.4	EDS spectra of the plane of the films (a) Y0, (b) Y02 and (c) Y08 thin films, respectively. Insets: the FESEM elemental distribution table of films.	90
Figure. 4.5	(a) The $\rho_{xx}$ versus $T$ plots of Y0, Y2, and Y8 thin films in the range of temperature $0 \text{ K} \leq T \leq 10 \text{ K}$ at zero magnetic field respectively. The inset graph shows $\rho_{xx}$ versus $T$ plots in the range of temperature $0 \text{ K} \leq T \leq 300 \text{ K}$ at zero magnetic field of Y0, Y2, and Y8 films, respectively, (b) variation of superconducting transition temperature ( $T_c$ ) and thin film lattice constant ( $a_t$ ) with Y concentration for the $Ho_{(1-x)}Y_xPdBi$ films. The inset depicts the $T_c$ vs $a_t$ plot of films.	91
Figure. 4.6	(a) $X'ac$ for driving fields of 0.10e, 0.50e, and 10e of Y8 film. Inset illustrate corresponding $X''ac$ , (b) The $\rho_{xx}$ vs temperature curve for Y8 thin film in the range of temperature of $2 \text{ K} \leq T \leq 10 \text{ K}$ at the different magnetic fields, (c) The slope estimates an upper critical field $H_{C2}(0)$ at absolute zero temperature $\sim 5.5T$ for Y8 film using Ginzburg-Landau (G-L) equation, (d) The extrapolated G-L fit (red solid line) yields the $H_{C2}(0)$ .	93
Figure. 4.7	The magneto-resistance curve at various temperatures for (a) Y0, (b) Y2, (c) Y8 films; (d-f) Magneto-conductance (MC) curves at various temperatures fitted with HLN mode for (d) Y0, (e) Y2, and (f) Y8 films; $l_\phi$ and $\alpha$ films extracted from HLN fit at 4K, 5K, 6K, 8K, and 10K for (g) Y0, (h) Y2, and (i)Y8.	95
Figure. 4.8	The combined power law fitting, $l_\phi^{-2}$ vs $T$ plots (a) for Y0 film, (b) for Y2 film, (c) for Y8 film. Inset: shows the $l_\phi \propto T^{-p/2}$ fit to obtain the p value for HYPB films.	96
Figure. 5.1	a) Gonio mode XRD pattern with Rietveld refinement of the polycrystalline bulk sample of $GdPdBi$ ; (b) Gonio-mode XRD pattern of the thin film of the $GdPdBi/Ta$ (5nm)/ $MgO$ substrate; inset: rocking curve along the (220) plane of the film; (c) Cross-sectional FESEM micrograph of the $GdPdBi$ thin film on the $Ta/MgO$ substrate; (d) EDS spectrum and elemental distribution of the film plane surface.	103
Figure. 5.2	(a-d) represents the SEM and Elemental color mapping images; (e) AFM image	105

depicting the surface roughness of GdPdBi thin film as  $\sim 5nm$ , of GdPdBi thin film.

- Figure. 5.3 (a) The MR of GdPdBi thin film at various temperature; (b) magneto-conductance  $\Delta G_{xx}$  as a function of the perpendicular component of the applied magnetic field  $H\cos\theta(T)$  at 6K in the field  $-3T \leq H(T) \leq 3T$ , where  $\Delta G_{xx}$  is defined as  $G_{xx}(H) - G_{xx}(0)$ . The inset illustrates the schematic of the measurement configuration, with  $\theta=0^\circ$  corresponds to the magnetic field being perpendicular to the sample surface. 106
- Figure. 5.4 (a) The HLN fitting curves plotted in solid black lines in field range  $\pm 2T$ ; (b) HLN fitted parameter  $\alpha$  in temperature regime  $1.9K \leq T(K) \leq 8K$ ; (c) The coherence length in temperature regime  $1.9K \leq T(K) \leq 8K$ , for GdPdBi thin films. 107
- Figure. 5.5 (a) The field dependent longitudinal electrical resistivity ( $\rho_{xx}$ ) of GdPdBi thin film with temperature, inset: Fitting of temperature dependent conductivity ( $\sigma$ ) data at 0T with semi-conducting channel in the range of temperature  $3.5 K \leq T \leq 300 K$ ; (b) The inverse of square of  $l_\varphi$  with respect to temperature represented in black symbols. 108

## LIST OF TABLES

Table. 1.1	Summary of the key observations in RPdBi alloys.	25
Table. 3.1	Summary of XRR simulated parameters, here $t_{\text{Ta}}$ and $t_{\text{YEPB}}$ are the thickness of Ta and $\text{Y}_{1-x}\text{Er}_x\text{PdBi}$ layers, $\sigma$ is the interface roughness, $\rho_{\text{Ta}}$ and $\rho_{\text{YEPB}}$ are the densities of Ta and $\text{Y}_{1-x}\text{Er}_x\text{PdBi}$ layers, respectively.	64
Table 3.2	Summary of electronic parameters of YEPB thin films obtained from fitting of the SdH oscillations data to Lifshitz–Kosevich theory. Here, $f$ : frequency of SdH oscillations; $n_{2D}$ : sheet carrier density; $m^*$ : effective mass of carriers; $k_F$ : Fermi wave vector; $v_F$ : Fermi velocity; $E_f^s$ : position of linear dispersion node from Fermi level; $T_D$ : Dingle temperature; $\Gamma$ : LL broadening; $\tau$ : transport lifetime, $l$ : mean free path; $\mu_s$ : quantum mobility of carriers; $2\pi\beta$ : Berry phase.	73
Table. 4.1	HLN fit values $\alpha$ and $l_\phi$ for HYPB films.	95
Table. 4.2	The obtained value of $l_\phi(0)$ , $A_{e-e}$ and $A_{e-ph}$ for Y0, Y2 and Y8 HYBN films.	96
Table. 5.1	The extracted HLN parameters at different temperatures in the magnetic field range $-2T < H(T) < 2T$ .	108